Heat Transfer and Fluid Flow during Electron Beam Welding of 304L Stainless Steel Alloy

Models were used to calculate the three-dimensional temperature field and fluid velocities for electron beam welding of 304L stainless steel

BY R. RAI, T. A. PALMER, J. W. ELMER, AND T. DEBROY

ABSTRACT

A numerical model for three-dimensional heat transfer and fluid flow in keyhole mode electron beam welding was developed and applied to 304L stainless steel welds made at different power density distributions achieved by varying the focal spot radius at a fixed input power. The model first calculates keyhole geometry based on energy balance on keyhole walls and then solves the three-dimensional temperature field and fluid velocities in the workpiece. Since the energy balance and, consequently, the keyhole penetration are affected by the keyhole wall temperatures, the variation of the keyhole wall temperature with depth has been considered. A modified turbulence model based on Prandtl's mixing length hypothesis was used to calculate the spatially variable effective values of thermal conductivity and viscosity to account for enhanced heat and mass transfer due to turbulence in the weld pool. Unlike models available in literature, the model proposed in this work considers the physical processes like variations of keyhole wall temperatures with depth and the resulting influence on calculation of keyhole depth and fluid velocities along the keyhole wall, and three-dimensional heat and mass transport. Thus, the model can be applied to materials with a range of thermophysical properties. The model was used to study the fluid flow patterns in the weld pool and their effects on the calculated weld geometry. The calculated weld dimensions agreed reasonably well with the measured values. Peclet number calculation showed that convective heat transfer was very significant. The influence of convection was illustrated by comparing the calculated weld pool geometries in the presence and absence of convection. The vapor pressures and wall temperatures in the keyhole increased with increase in the peak power density.

R. RAI, T. A. PALMER, and T. DEBROY are with Department of Materials Science and Engineering, The Pennsylvania State University, University Park, Pa. J. W. ELMER is with Lawrence Livermore National Laboratory, Livermore, Calif.

Introduction

High-energy-density electron beams are often used to join a wide range of materials with an equally wide range of thicknesses for applications where a high aspect ratio (depth/width) and narrow heat-affected zone are needed. Due to the very high intensity of electron beams, the workpiece material undergoes strong localized evaporation, resulting in the formation of a narrow and deep vapor cavity or "keyhole" (Refs. 1, 2). A pressure gradient forms along the keyhole depth because of the flow of metal vapor resulting in a variation in the equilibrium temperatures of the keyhole walls with weld depth. Temperatures at the top and the bottom of the keyhole can differ by several hundred degrees (Ref. 3), which results in the flow of liquid metal in the vertical direction under the influence of the surface-tension gradient along the keyhole walls.

While many numerical models for heat transfer and fluid flow have been developed for keyhole mode laser welding (Refs. 4–23), comprehensive heat transfer and fluid flow models for electron beam welding are not available in the literature. Klemens (Ref. 7) performed pressure balance at the keyhole walls to calculate the keyhole radius. Mazumder and Steen (Ref. 8) proposed a 3-D heat conduction model for the calculation of temperature profiles in the workpiece. Kaplan (Ref. 12) and Zhao (Ref. 19) calculated the asymmetric keyhole profile at high welding speeds by considering energy balance at the keyhole walls. Sudnik et al. (Ref. 13) approximated the 3-D fluid flow in the weld pool by 2-D flows in horizontal and vertical planes. Ki et al. (Refs. 17, 18) calculated the transient evolution of the keyhole and the weld pool during laser welding using the level set method to track the liquid-vapor interface. Rai et al. (Refs. 20–23) calculated the asymmetric keyhole profile through energy balance at keyhole walls considering multiple reflections of the laser beam within the keyhole, and the 3-D heat transfer and fluid flow in the weld pool. Elmer et al. (Ref. 24) proposed three heat conduction models for electron beam welding based on distributed, point, or line heat sources, depending on the power densities and compared calculated and measured weld geometries. Wei and Giedt (Ref. 25) proposed a two-dimensional heat transfer and fluid flow model and computed the free surface temperature, liquid layer thickness, and tangential free surface fluid velocities assuming the surface tension gradient to be the main driving force for the fluid flow. Wei and Chow (Ref. 26) studied the effect of beam focusing and alloying elements on the shape of the electron beam keyhole. Assuming the vapor cavity to be a paraboloid of revolution, Wei and Shian (Ref. 27) calculated penetration depth and surface temperatures using an analytical three-dimensional heat conduction model.

Here we propose a three-dimensional phenomenological model for heat transfer and fluid flow in electron beam welding that considers keyhole formation and the variation of keyhole wall temperature as a function of depth. A very important parameter in the electron beam welding

KEYWORDS

Electron Beam Welding
Keyhole
Heat Transfer
Fluid Flow
Stainless Steel
Weld Process Simulation
Three-Dimensional
Phenomenological Model

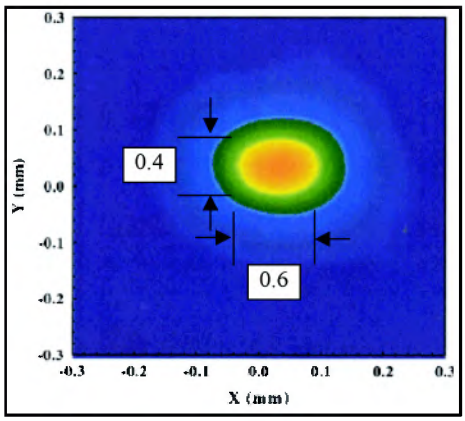

Fig. 1 — Beam shape for 0.17-mm beam radius produced at sharp focus settings for 1000-W power at a work distance of 229 mm.

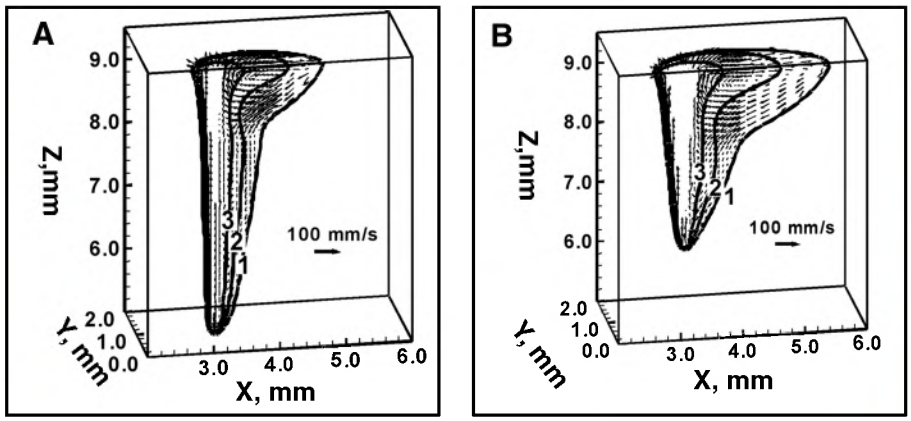

Fig. 2 — Fluid flow pattern in electron beam weld for focal spot radius of the following: A — 0.13 mm; B — 0.28 mm. Labels 1, 2, and 3 represent 1697, 1900, and 2200 K, respectively.

process is the power density distribution. In this work, the model was applied to welds made on 304L stainless steel with fixed input power and welding speed but different power density distributions. The power density distribution was varied by changing the work distance and then refocusing the electron beam to a sharp spot on the workpiece surface. The increase in the focal spot diameter with increasing work distance also affects the geometry of the weld pool shape (Ref. 28). The calculated and the experimental weld geometries were compared for each case and the effect of variation of power density distribution on the weld geometry was investigated. The resulting fluid flow circulation patterns in the 304L stainless steel electron beam weld pools were studied. The nail-head-shaped weld cross section of electron beam welds observed in this study was explained in terms of the fluid flow and resulting convective heat transfer.

Experiments

Autogenous electron beam welds were made on 9.5-mm-thick 304L stainless steel samples with a power of 1000 W (100 kV, 10 mA) and a welding speed of 17 mm/s. The stainless steel workpiece had a composition of 18.2%Cr, 8.16%Ni, 1.71%Mn, 0.02%C, 0.082%N, 0.47%Mo, 0.44%Si, 0.14%Co, 0.35%Cu, 0.0004%S, 0.03%P, and balance Fe. Six welds were made using a sharply focused beam at different work distances (Table 1). The resulting weld pool cross sections were polished and etched with electrolytic oxalic acid solution to provide the outline of the fusion zone boundary. Image Pro, Version 4.1 was then used to measure the weld dimensions (Ref. 28).

The sharp focus condition was determined by using an enhanced modified Faraday cup (EMFC) device to ensure a more consistent and quantified beam focus than is manually possible (Ref. 28). The EMFC device samples the electron beam through 17 linear slits placed radially around a tungsten slit disk and converts them into voltage drops across the known resistor. A computer-assisted tomographic (CT) imaging algorithm is then used to reconstruct the power density distribution of the beam using the data from the 17 linear slits. From the reconstructed beam, the peak power density, full width of the beam at half of its peak intensity (FWHM), and the full width of the beam at $1/e^2$ of the peak intensity (FWe2) are measured. The beam radius was taken to be ½ of the FWe2 value measured by the EMFC. Figure 1 shows the beam shape for the case of a 0.17-mm focal spot radius, from EB welding machine model number SN/175 manufactured by Hamilton Standard at a 229-mm work distance (Ref. 28). Since the beam has an elliptical shape, the effective value of the beam radius was taken as the radius of a circle with an area equal to the actual beam spot (Ref. 28). The beam shape and radius may vary with distance from the focal plane, which can affect the weld geometry. However, due to a lack of data on the divergence of the beam near the focal plane, its effect has been neglected in this work.

Mathematical Model

Calculation of Keyhole Profile

Quasi-steady state and flat top surface outside the keyhole region are assumed. The fluctuations of the keyhole shape and size have been neglected. Energy balance is performed on the liquid-vapor interface to calculate the keyhole geometry using a model that is available in literature (Refs.

Table 1 — Experimental and Calculated Weld Dimensions for Welds Made at 1000-W Input Power and 17 mm/s Welding Speed Using Electron Beam Welding Machine S/N 175

WD mm	R_f mm	PPD kW/mm²	d_m mm	d_c mm	% error	w_m mm	w_c mm	% error	MA mm²	AR
127	0.131	34.9	4.46	4.20	–6.19	1.27	1.38	7.97	2.40	3.52
184	0.166	21.6	4.21	3.87	–8.79	1.29	1.52	15.13	2.55	3.27
229	0.173	20.0	3.97	3.80	–4.47	1.48	1.58	6.33	2.63	2.65
305	0.207	14.1	3.69	3.56	–3.65	1.48	1.68	11.90	2.58	2.49
381	0.243	10.2	3.39	3.33	–1.80	1.55	1.76	11.93	2.56	2.19
457	0.279	7.79	2.96	2.97	0.34	1.71	1.90	10.00	2.62	1.73

WD; work-distance, R_f: radius of focal spot; PPD: peak power density; d; depth; w: width; subscripts m and c stand for measured and calculated; MA: melted cross-sectional area; AR: aspect ratio.

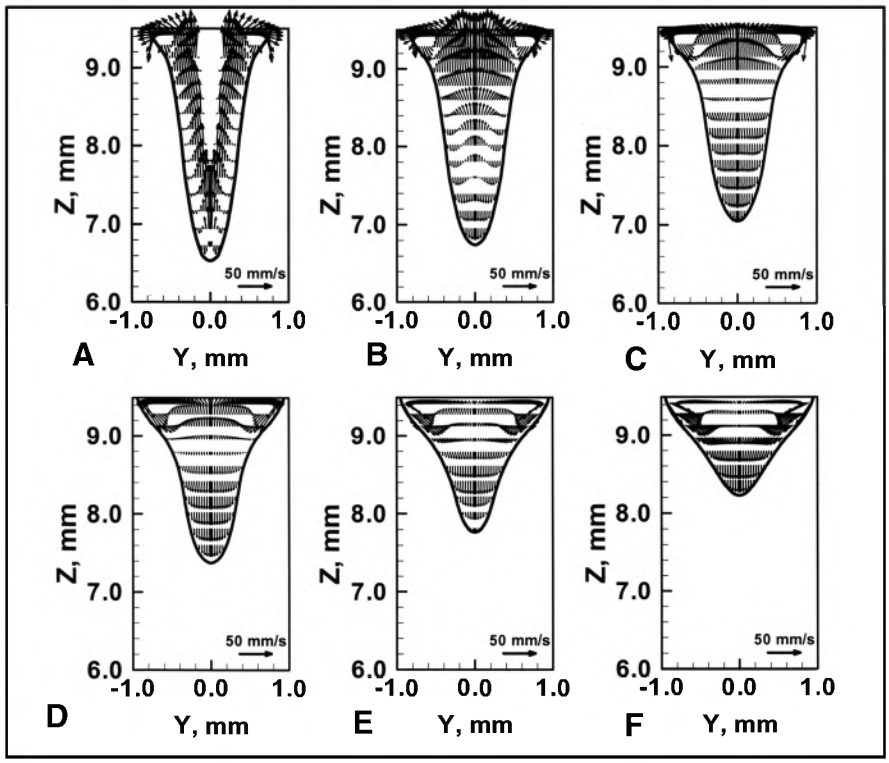

Fig. 3 — Fluid flow in the weld made with 0.28-mm beam radius in transverse planes at the following locations behind the electron beam: A — 0.11 mm; B — 0.28 mm; C — 0.45 mm; D — 0.62 mm; E — 0.78 mm; and F — 0.95 mm. Only the top 3.5 mm of the total plate thickness of 9.5 mm is shown.

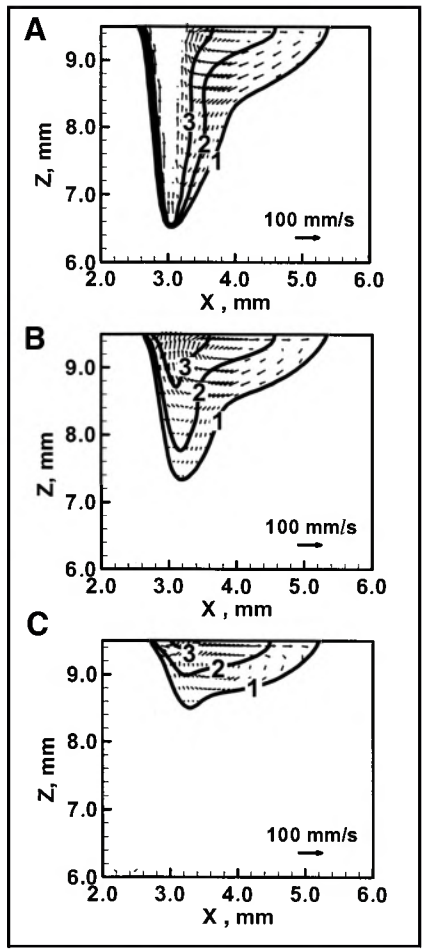

Fig. 4 — Fluid flow in the weld made with 0.28-mm beam radius in longitudinal planes at the following locations from the centerline: A — 0 mm; B — 0.28 mm; and C — 0.45 mm. Labels 1, 2, and 3 represent 1697, 1900, and 2200 K, respectively. Only the top 3.5 mm of the total plate thickness of 9.5 mm is shown.

12, 19–23). The temperature gradient in the vertical direction is small compared to that along any direction in the horizontal plane. Therefore, the heat transfer takes place mainly along horizontal planes. However, the temperature gradient on the keyhole walls along the vertical direction is still sufficient to generate surface tension driven flow along the keyhole walls in the vertical direction.

The keyhole is kept open by a balance between the surface tension force $\gamma/r(z)$, the hydrostatic force due to the liquid head ρgz, and the vapor pressure inside the keyhole p through the following relationship:

$$p = \rho gz + \gamma(T)/r(z) \qquad (1)$$

where ρ is the density, g is the acceleration due to gravity, $\gamma(T)$ is the surface tension at temperature T, and r(z) is the keyhole radius at distance z from the top surface. The decrease in r(z) with increasing depth in the keyhole results in an increase in the surface tension force. As a result, the vapor pressure required to keep the keyhole open increases with depth. Thus, the vapor pressure at various depths in the keyhole can be calculated from the above equation.

The temperature at the keyhole wall at any depth can then be calculated from the equilibrium temperature vs. pressure relation for the alloy-vapor interface assuming ideal solution behavior (Ref. 29). The keyhole geometry is iteratively calculated first by assuming a constant temperature equal to the normal boiling point of the alloy at 1 atmosphere on the keyhole walls. The calculation of the energy balance at the keyhole walls is described elsewhere (Refs. 12, 19–23). The wall temperature is modified in subsequent iterations by first calculating the vapor pressure required to balance the surface tension and the hydrostatic force at the keyhole wall. Using this calculated vapor pressure, the wall temperature is then determined through equilibrium temperature vs. pressure relation, changing the keyhole depth and radius. Thus, the wall temperatures are corrected with each iteration, and the calculations continue until the change in keyhole depth with each additional iteration becomes less than 10^{-4} mm, at which point the calculations are assumed to con-

Table 2 — Data Used for Calculations

Physical Property	Value
Solidus temperature, (K) [Refs. 23, 48]	1697
Liquidus temperature, (K) [Refs. 23, 48]	1727
Density of liquid (kg/m^3) [Ref. 23]	7000
Specific heat of solid, (J/kg K) [Ref. 23]	712
Specific heat of liquid, (J/kg K) [Ref. 23]	800
Viscosity, (Pa-s) [Ref. 23]	0.007
Coefficient of thermal expansion, (1/K) [Ref. 23]	1.96×10^{-5}
Temperature coefficient of surface tension, (N/m K) [Ref. 48]	-0.43×10^{-3}
Enthalpy of solid at melting point, (J/kg) [Refs. 23, 48]	1.20×10^{6}
Enthalpy of liquid at melting point, (J/kg) [Refs. 23, 48]	1.26×10^{6}
Emissivity	0.3
Heat transfer coefficient, W/m^2-K	210
Plasma attenuation coefficient, (m^{-1})	10
Absorption coefficient	0.2

Values are estimated based on the data available in the reference.

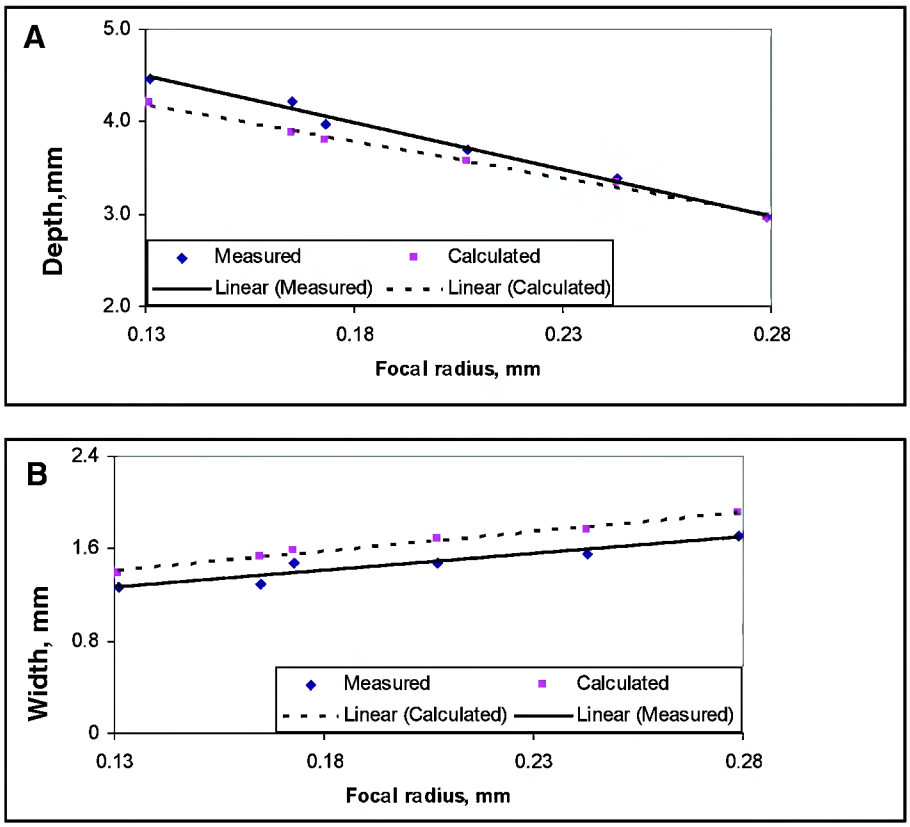

Fig. 5 — A — Variation of weld depth with spot radius; B — variation of weld width with spot radius.

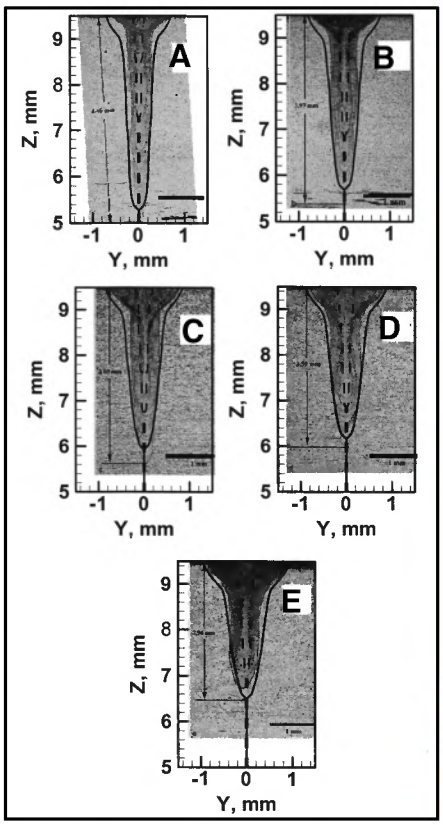

Fig. 6 — Comparison of experimental and calculated weld geometries for focal spot radii: A — 0.131 mm; B — 0.173 mm; C — 0.207 mm; D — 0.243 mm; E — 0.279 mm. Input power: 1000 W. Welding speed: 17 mm/s.

verge. During calculation of the asymmetric keyhole geometry, all temperatures inside the keyhole were assigned the wall temperature at that depth, for the identification of the keyhole. At each horizontal *xy* plane, where x is the direction of welding, the keyhole boundary was identified by both minimum and maximum *x* values for any given *y* value.

The attenuation of the beam due to absorption and scattering, as it traverses a unit distance in the plasma, is estimated by using attenuation coefficients (Ref. 12). The beam attenuation affects the amount of electron beam energy incident on keyhole walls below the workpiece surface. It is assumed that the energy loss due to large angle backscattering of electrons by the plasma in a deep, narrow keyhole is small (Ref. 30). Consequently, a small value of attenuation coefficient has been assumed here for the attenuation of the electron beam. With a plasma attenuation coefficient value of 10/m used for electron beam plasma here, 99% and 96% of the electron beam passes through lengths of 1 and 4 mm, respectively, through the plasma. Table 2 lists the values of material properties and process parameters used for the calculations. Thermal conductivity values for the solid phase were temperature dependent and the thermal conductivity data were available up to a temperature of 1273 K. Approximate thermal conductivity values above this temperature were estimated based on linear extrapolation of the experimental data for 304L stainless steel (Ref. 31). Thermal conductivity for liquid was calculated based on the Wiedemann-Franz relation, which states that the ratio of thermal conductivity to the product of temperature and electrical conductivity is a constant (Ref. 32). The electrical conductivity of liquid stainless steel was taken as the electrical conductivity of liquid iron at its theoretical melting point, which was close to the value obtained by extrapolating the data for electrical resistivity of 18Cr-8Ni steel between 300 and 1273 K to the liquidus temperature (Ref. 29).

Heat Transfer and Fluid Flow in the Weld Pool

After calculating the keyhole profile, the fluid flow and heat transfer in the weld pool are modeled by solving the equations of conservation of mass, momentum, and energy in three dimensions. The liquid metal flow in the weld pool can be represented by the following momentum conservation equation (Refs. 33, 34):

$$\rho\frac{\partial u_j}{\partial t}+\rho\frac{\partial\left(u_i u_j\right)}{\partial x_i}=\frac{\partial}{\partial x_i}\left(\mu\frac{\partial u_j}{\partial x_i}\right)+S_j \qquad (2)$$

where ρ is the density, *t* is the time, x_i is the distance along the i^{th} (i = 1, 2, and 3) orthogonal direction, u_j is the velocity component along the *j* direction, μ is the effective viscosity, and S_j is the source term for the j^{th} momentum equation and is given as

$$S_j=-\frac{\partial p}{\partial x_j}+\frac{\partial}{\partial x_i}\left(\mu\frac{\partial u_i}{\partial x_j}\right)-C\left(\frac{\left(1-f_L\right)^2}{f_L^3+B}\right)u_j+\rho g_j\beta\left(T-T_{ref}\right)-\rho U\frac{\partial u_j}{\partial x_1} \qquad (3)$$

where *p* represents pressure, *U* is the weld-

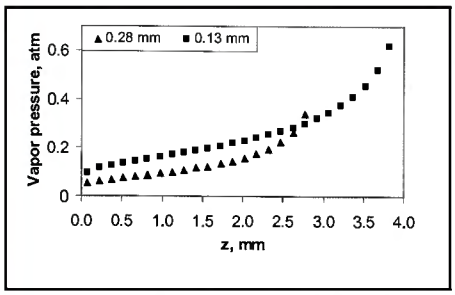

Fig. 7 — Variation of vapor pressure in the keyhole with depth for radius of 0.13 and 0.28 mm. z = 0 at the surface of the workpiece.

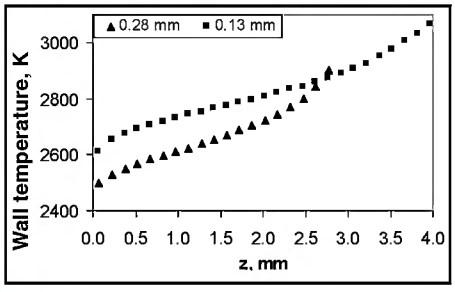

Fig. 8 — Variation of keyhole wall temperature with depth for radius of 0.13 and 0.28 mm. z = 0 at the surface of the workpiece.

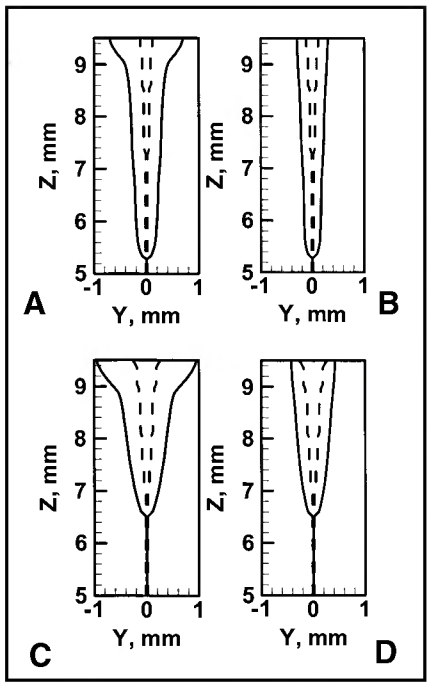

Fig. 9 — Weld pool cross sections for focal spot radius of 0.13 mm: A — With convection and B — without convection; and 0.28 mm: C — with convection and D — without convection. Input power: 1000 W, welding speed: 17 mm/s.

ing velocity, β is the coefficient of volume expansion, and T_{ref} is a reference temperature taken here as the solidus temperature. The third term represents the frictional dissipation in the mushy zone according to the Carman-Kozeny equation for flow through a porous media (Refs. 35, 36), where f_L is the liquid fraction, B is a very small computational constant introduced to avoid division by zero, and C is a constant accounting for the mushy zone morphology (a value of 1.6×10^4 was used in the present study) (Ref. 36). The fourth term is the buoyancy source term (Refs. 37–41). The last term accounts for the relative motion between the electron beam and the workpiece (Ref. 37).

The following continuity equation is solved in conjunction with the momentum equation to obtain the pressure field.

$$\frac{\partial\left(\rho u_i\right)}{\partial x_i} = 0 \qquad (4)$$

In order to trace the weld pool liquid/solid interface, i.e., the phase change, the total enthalpy H is represented by a sum of sensible heat h and latent heat content ΔH, i.e., H = h + ΔH (Ref. 37). The sensible heat 'h' is expressed as $h=\int C_p dT$, where C_p is the specific heat, and T is the temperature. The latent heat content ΔH is given as $\Delta H = f_L L$, where L is the latent heat of fusion. The liquid fraction f_L is assumed to vary linearly with temperature for simplicity (Ref. 37):

$$f_L = \begin{cases} 1 & T > T_L \\ \dfrac{T - T_S}{T_L - T_S} & T_S \le T \le T_L \\ 0 & T < T_S \end{cases} \qquad (5)$$

where T_L and T_S are the liquidus and solidus temperatures, respectively. Thus, the transport of thermal energy in the weld workpiece can be expressed by the following modified energy equation:

$$\rho\frac{\partial h}{\partial t} + \rho\frac{\partial\left(u_i h\right)}{\partial x_i} = \frac{\partial}{\partial x_i}\left(\frac{k}{C_p}\frac{\partial h}{\partial x_i}\right) + S_h \qquad (6)$$

where k is the thermal conductivity. The source term S_h is due to the latent heat content and is given as

$$S_h = -\rho\frac{\partial\left(\Delta H\right)}{\partial t} - \rho\frac{\partial\left(u_i \Delta H\right)}{\partial x_i} - \rho U\frac{\partial h}{\partial x_1} - \rho U\frac{\partial \Delta H}{\partial x_1} \qquad (7)$$

The heat transfer and fluid flow equations were solved for the complete workpiece. For the region inside the keyhole, the coefficients and source terms in the discretized algebraic equations were adjusted to obtain zero fluid velocities and temperature equal to the wall temperature at that depth. The methodology for the implementation of known values of variables in any specified location of the solution domain is well documented in the literature (Ref. 34).

Boundary Conditions

A 3-D Cartesian coordinate system is used in the calculation, and only half of the workpiece is considered since the weld is symmetrical about the weld centerline. The boundary conditions are discussed as follows.

Top Surface

Outside the region of vapor cavity, the weld top surface is assumed to be flat. The velocity boundary conditions are given as (Refs. 40–43)

$$\mu\frac{\partial u}{\partial z} = f_L\frac{d\gamma}{dT}\frac{\partial T}{\partial x}$$
$$\mu\frac{\partial v}{\partial z} = f_L\frac{d\gamma}{dT}\frac{\partial T}{\partial y}$$
$$w = 0 \qquad (8)$$

where u, v, and w are the velocity components along the x, y, and z directions, respectively, and $d\gamma/dT$ is the temperature coefficient of surface tension. As shown in this equation, the u and v velocities are determined from the Marangoni effect (Refs. 40–43). The w velocity is equal to zero since the outward flow at the top surface is assumed to be negligible.

The heat flux at the top surface is given as

$$k\left.\frac{\partial T}{\partial z}\right|_{top} = \frac{fQ\eta}{\pi r_b^2}exp\left(-\frac{f\left(x^2+y^2\right)}{r_b^2}\right) - \sigma\varepsilon\left(T^4 - T_a^4\right) - h_c\left(T - T_a\right) - \sum_{i=1} h_{v,i} J_{v,i} \qquad (9)$$

where r_b is the beam radius, f (=3.0) is the power distribution factor, Q is the total power, η is the absorption coefficient, σ is the Stefan-Boltzmann constant, ε is the emissivity, h_c is the heat transfer coefficient, $h_{v,i}$ is the heat of evaporation for the i^{th} element, $J_{v,i}$ is the evaporation flux for the i^{th} element calculated using the Langmuir equation (Ref. 1), and T_a is the ambient temperature. In Equation 9, the first term on the right-hand side is the heat input from the Gaussian heat source. The

second, third, and fourth terms represent the heat loss by radiation, convection, and vaporization, respectively.

Symmetric Plane

The boundary conditions are defined as zero flux across the symmetric surface, i.e., the vertical plane defined by the welding direction, as

$$\frac{\partial u}{\partial y}=0,\ v=0,\ \frac{\partial w}{\partial y}=0 \qquad (10)$$

$$\frac{\partial h}{\partial y}=0 \qquad (11)$$

Keyhole Surface

$$h = h_w \qquad (12)$$

where h_w is the sensible heat of the material at the local wall temperature. The velocity component perpendicular to the keyhole surface is assigned zero to represent no mass flux due to convection. Along the keyhole walls, the temperature gradient in the vertical direction results in the surface tension gradient. As a result, Marangoni convection currents are formed in the vertical direction along the surface of the keyhole. The w-velocity boundary condition along the keyhole walls is therefore given as

$$\mu\frac{\partial w}{\partial n}=f_L\frac{d\gamma}{dT}\frac{\partial T}{\partial z} \qquad (13)$$

where n is the direction vector normal to the keyhole surface.

Solid Surfaces

At all solid surfaces far away from the heat source, a convective heat transfer boundary condition is given and the velocities are set to be zero.

Turbulence Model

The presence of fluctuating velocities during welding often enhances the rates of transport of heat, mass, and momentum in the weld pool. An appropriate turbulence model that provides a systematic framework for calculating effective viscosity and thermal conductivity (Refs. 41, 42) is used to account for the fluctuating velocities. The values of these properties vary with the location in the weld pool and depend on the local characteristics of the fluid flow. In this work, a turbulence model based on Prandtl's mixing length hypothesis is used to estimate the turbulent viscosity (Ref. 45)

$$\mu_t = \rho l_m v_t \qquad (14)$$

where μ_t is the turbulent viscosity, l_m is the mixing length, and v_t is the turbulence velocity. The mixing length at any location within the weld pool is the distance traveled by an eddy before its decay and is often taken as the distance from the nearest wall (Ref. 45). The extent of computed turbulent kinetic energy was found to be about 10% of the mean kinetic energy, in a controlled numerical study of recirculating flows in a small square cavity (Ref. 46). Yang and DebRoy (Ref. 47) computed mean velocity and turbulent energy fields during GMA welding of HSLA 100 steel using a two equation k-ε model. Their results also show that there is a 10% contribution of the turbulent kinetic energy to the mean kinetic energy. The turbulent velocity v_t can therefore be expressed as

$$v_t=\sqrt{0.1v^2} \qquad (15)$$

By coupling Equations 14 and 15, the turbulent viscosity can be expressed as

$$\mu_t = 0.3\rho l_m v \qquad (16)$$

The effective viscosity at a particular point can be expressed as the sum of the turbulent (μ_t) and laminar (μ_l) viscosities, i.e., $\mu = \mu_t + \mu_l$. The corresponding local turbulent thermal conductivities are calculated by using the turbulent Prandtl number, which is defined in the following relationship:

$$Pr=\frac{\mu_t c_p}{k_t} \qquad (17)$$

where k_t is the turbulent thermal conductivity. For the calculations described here, the turbulent thermal conductivity is calculated by assuming a Prandtl number of 0.9, based on previous modeling work (Refs. 44, 46).

Calculation Methodology

The calculation of heat transfer and fluid flow in the workpiece was done in the following steps:

1. The keyhole geometry is calculated based on a heat balance model available in the literature (Ref. 17) and boiling point temperature at all locations on the keyhole wall.
2. The vapor pressure in the keyhole is calculated at all depths through a force balance between the vapor pressure, surface tension, and hydrostatic force.
3. Wall temperatures are calculated for all depths from the equilibrium pressure-temperature relations for the given alloy.
4. Keyhole geometry is calculated assuming new values of wall temperatures at different depths.
5. Steps 2–4 are repeated until the variation of keyhole depth with further iteration becomes less than 10^{-4} mm.
6. The keyhole geometry is mapped onto a coarser mesh for 3-D heat transfer and fluid flow calculations. Temperatures are assigned on the keyhole wall from the values calculated during keyhole geometry calculation based on equilibrium pressure-temperature relations for the alloy.
7. The momentum and energy balance equations are solved keeping fixed temperatures on the keyhole wall, and assuming no mass flux across the wall boundary. Convergence was assumed when residuals of enthalpy and u, v, and w velocities are less than 1%.
8. A turbulence model is used to update the viscosities and thermal conductivities in the liquid phase.

Results and Discussion

Figure 2 shows the computed weld geometry and the 3-D fluid flow within the weld pool for the welds made with the highest (0.28 mm) and the lowest (0.13 mm) beam radii at input power of 1000 W and welding speed of 17 mm/s. The flow of molten metal is driven by the surface tension gradient along the keyhole walls and on the top surface of the weld pool. A negative temperature coefficient of surface tension drives fluid flow at the top surface from the high-temperature region near the keyhole to the low-temperature region near the solid-liquid boundary, resulting in enhanced heat transfer at the top surface.

Within the keyhole, temperatures are highest at the bottom and lowest near the top surface. This temperature gradient along the keyhole surface drives fluid flow from the hot keyhole bottom to the top, resulting in a fluid flow pattern in the weld pool where hot fluid moves along the keyhole walls to the top, moving outward from there, and finally coming back inward and down along the solid-liquid boundary. A distinct nail-head shape results from this type of fluid flow pattern.

Figure 3 shows the fluid flow in transverse planes perpendicular to the welding direction at selected distances from the heat source. Plane 'a' is the closest to the electron beam location (0.11 mm) and plane 'f' is the farthest behind the electron beam (0.95 mm). The keyhole region, which is characterized by the absence of velocity vectors at the center of the weld pool, is present only in Fig. 3A. Under the influence of surface-tension gradients at the vapor-liquid interface, the fluid near the keyhole wall moves from the bottom to the top. The magnitude of fluid velocities in the vertical direction is highest near the vapor-liquid interface and decreases to zero at the solid-liquid boundary. As the

distance of the transverse section from the heat source increases, fluid gradually starts to come downward and the reversal of the direction of fluid velocity from upward to downward happens at shorter distances from the top surface.

In the longitudinal sections shown in Fig. 4, the fluid moves upward near the heat source location and circulates backward near the top surface resulting in enhanced heat transfer toward the rear of the weld pool and an elongated weld pool. The circulation pattern is similar in all of the longitudinal sections shown in Fig. 4 located at different distances from the weld centerline.

As shown in Table 1, an increase in work distance from 127 to 457 mm resulted in more than a twofold increase in the beam focal spot radius (R_f). With a larger focal spot radius, the beam is more diffuse and the peak power density is lower, decreasing from 34.9 kW/mm^2 for 127-mm work distance (focal radius = 0.13 mm) to 7.79 kW/mm^2 for 457-mm work distance (focal radius = 0.28 mm) (Ref. 28). As a result, the weld characteristics are likely to be strongly affected by the variation in beam radius. Figure 5A, B shows the variation of weld pool depth and width at the top surface, respectively, with the variation in the focal spot radius. The calculated weld width and depth display trends similar to the measured values. With an increase in beam radius, the input energy distribution is more diffuse and the peak power density decreases, thus decreasing the weld penetration. However, a larger focal spot radius increases melting on the top surface, resulting in a wider weld pool. Thus, the ratio of weld pool depth to width decreases with increasing beam radii, as shown in Table 1. The area of calculated weld cross section is nearly constant with variation in the beam radius.

Figure 6 shows the comparison of calculated and experimental weld cross sections for different focal spot radii. The dashed lines show the calculated keyhole profile. The calculated keyhole radius at the top surface of the weld is closely related to the electron beam radius. The calculated weld cross sections are similar to the experimentally observed weld cross sections. The experimentally observed nail-head shape of the weld cross section is predicted by calculations as well. Even though the beam divergence may contribute to the nail-head shape, this characteristic shape of electron beam welds can also be explained in terms of Marangoni convection.

The keyhole and weld geometry depends on the keyhole wall temperatures, which in turn depend on the vapor pressure in the keyhole. Figure 7 shows the variation of vapor pressure with depth for beam radii of 0.13 and 0.28 mm. For the welds shown in Fig. 6, the keyhole becomes narrower and deeper as the beam radius is decreased. The narrower keyhole for lower focal spot radius requires a larger vapor pressure to balance the surface tension force that tends to close the keyhole. Therefore, vapor pressures are higher for the higher peak power densities obtained with the smaller focal spot radii. In accordance with higher vapor pressures in the keyhole for the smaller beam radius, equilibrium wall temperatures at the keyhole walls are higher for the beam radius of 0.13 mm as compared to the larger beam radius of 0.28 mm as shown in Fig. 8. The higher keyhole wall temperatures calculated for the smaller focal spot radius are consistent with more intense heating. The average temperature gradient in the perpendicular-to-welding direction was always significantly higher than that along the keyhole wall in the vertical direction. For example, for the weld made with the beam radius of 0.28 mm, the average temperature gradient in the weld pool at mid-height of the keyhole in the horizontal direction was about 26 times that in the vertical direction. Thus, the assumption that the temperature gradient in the vertical direction is small compared to that in the horizontal plane is justified. Since the variation of vapor pressure from the bottom to the top of the keyhole results in less than a 15% variation in the wall temperature, any errors in vapor pressure calculation are likely to result in much smaller errors in the computed wall temperatures.

The significance of convective heat transfer relative to conductive heat transfer is given by the Peclet number, $Pe=\rho u C_p(w/2)/k$, where ρ is the density, u is the characteristic velocity, C_p is the specific heat, w is the weld pool width, and k is the thermal conductivity. Using ρ = 7000 kg/m^3, u = 0.1 m/s (the value of reference velocity vector in Fig. 2), C_p = 800 J/kg-K, w/2 = 8.0 × 10^{-4} m, and k = 30 W/m-K, Pe = 14.9. Therefore, convective heat transfer is very important for the welding conditions studied here.

To further illustrate the significance of convection on the weld pool geometry, the temperature field in the workpiece was calculated by considering only conductive heat transfer and ignoring fluid flow. Figure 9A, C shows the calculated weld pool cross sections for the case of 0.13- and 0.28-mm focal spot radius, respectively, with convection, and Fig. 9B, D shows the corresponding weld cross sections in the absence of any convection. In the absence of convection, heat transfer is significantly reduced, which results in much narrower weld pools. The calculated weld pool in absence of convection also lacks the nail head shape usually observed in experiments because of the absence of enhanced outward heat transfer at the top surface of the workpiece. The differences in shape and size of the calculated weld pools in absence of and in the presence of convection indicate the significance of convective heat transfer under the conditions considered.

Summary and Conclusions

The geometry of the keyhole formed during electron beam welding was calculated through an energy balance at the keyhole walls considering the variation of vapor pressure and keyhole wall temperature with depth. A numerical heat transfer and fluid flow model was used to calculate the three-dimensional temperature field and fluid velocities for electron beam welding of 304L stainless steel. A turbulence model based on Prandtl's mixing length hypothesis was used to estimate the effective viscosities and thermal conductivities in the weld pool. The vapor pressure in the keyhole was calculated through a force balance on the keyhole wall considering the surface tension force, the hydrostatic force, and the force due to vapor pressure. The wall temperatures were calculated from equilibrium temperature-pressure relations for the alloy.

The calculated weld pool depth and width were compared with experimentally observed values for a set of experiments where the power density distribution was varied by changing the focal spot radius at a fixed input power. As the focal spot size increased and the power distribution became progressively diffuse, the penetration depth decreased and the weld width increased proportionally in order to maintain the total weld cross-sectional area for the fixed input power. Higher peak power density with the same input power resulted in higher peak temperature and vapor pressure at the keyhole bottom. Fluid circulation in the weld pool was studied for transverse sections located at different distances from the electron beam. Convective heat transfer was very significant in determining the weld geometry, as shown by Peclet number calculations. In the absence of convection, the calculated nail head shape of the weld pool was not obtained. The reduced heat transfer near the top surface in the absence of convection resulted in a much narrower calculated weld pool, further illustrating the significance of convective heat transfer for the conditions of welding considered.

Acknowledgment

The work was supported by a grant from the U.S. Department of Energy, Office of Basic Energy Sciences, Division of Materials Sciences, under grant number DE-FGO2-01ER45900.

References

1. DebRoy, T., and David, S. A. 1995. Physical processes in fusion welding. *Reviews of Modern Physics* 67: 85–112.

2. David, S. A., and DebRoy, T. 1992. Current issues and problems in welding science. *Science* 257: 497–502.

3. Schauer, D. A., Giedt, W. H., and Shintaku, S. M. 1978. Electron beam welding cavity temperature distributions in pure metals and alloys. *Welding Journal* 57(5): 127-s to 133-s.

4. Klein, T., Vicanek, M., Kroos, J., Decker, I., and Simon, G. 1994. Oscillations of the keyhole in penetration laser beam welding. *Journal of Physics D: Applied Physics* 27: 2023–2030.

5. Swift-Hook, D. E., and Gick, A. E. F. 1973. Penetration welding with lasers. *Welding Journal* 52: 492-s to 499-s.

6. Andrews, J. G., and Atthey, D. R. 1976. Hydrodynamic limit to penetration of a material by a high power beam. *Journal of Physics D: Applied Physics* 9: 2181–2194.

7. Klemens, P. G. 1976. Heat balance and flow conditions for electron beam and laser welding. *Journal of Applied Physics* 47: 2165–2174.

8. Mazumder, J., and Steen, W. M. 1980. Heat transfer model for cw laser material processing. *Journal of Applied Physics* 51: 941–947.

9. Postacioglu, N., Kapadia, P., Davis, M., and Dowden J. 1987. Upwelling in the liquid region surrounding the keyhole in penetration welding with a laser. *Journal of Physics D: Applied Physics* 20: 340–345.

10. Kroos, J., Gratzke, U., and Simon, G. 1993. Towards a self-consistent model of the keyhole in penetration laser beam welding. *Journal of Physics D: Applied Physics* 26: 474 to 480.

11. Metzbower, E. A. 1993. Keyhole formation. *Metallurgical Transactions B* 24: 875–880.

12. Kaplan, A. 1994. A model of deep penetration laser welding based on calculation of the keyhole profile. *Journal of Physics D: Applied Physics* 27: 1805–1814.

13. Sudnik, W., Radaj, D., and Erofeew, W. 1996. Computerized simulation of laser beam welding, modelling and verification. *Journal of Physics D: Applied Physics* 29: 2811–2817.

14. Matsunawa, A., and Semak, V. 1997. The simulation of front keyhole wall dynamics during laser welding. *Journal of Physics D: Applied Physics* 30: 798–809.

15. Solana, P., and Ocana, J. L. 1997. A mathematical model for penetration laser welding as a free-boundary problem. *Journal of Physics D: Applied Physics* 30: 1300–1313.

16. Pastor, M., Zhao, H., Martukanitz, R. P., and DebRoy, T. 1999. Porosity, underfill and magnesium loss during continuous wave Nd:YAG laser welding of thin plates of aluminum alloys 5182 and 5754. *Welding Journal* 78(6): 207-s to 216-s.

17. Ki, H., Mohanty, P. S., and Mazumder, J. 2002. Modeling of laser keyhole welding: Part I. Mathematical modeling, numerical methodology, role of recoil pressure, multiple reflections, and free-surface evolution. *Metallurgical and Materials Transactions A* 33A: 1817 to 1830.

18. Ki, H., Mohanty, P. S., and Mazumder, J. 2002. Simulation of keyhole evolution, velocity, temperature profile, and experimental verification. *Metallurgical and Materials Transactions A*, 33A: 1831–1842.

19. Zhao, H., and DebRoy, T. 2003. Macroporosity free aluminum alloy weldments through numerical simulation of keyhole mode laser welding. *Journal of Applied Physics* 93: 10089 to 10096.

20. Rai, R. and DebRoy, T. 2006. Tailoring weld geometry during keyhole mode laser welding using a genetic algorithm and a heat transfer model. *Journal of Physics D: Applied Physics* 39: 1257 to 66.

21. Rai, R., Roy, G. G., and DebRoy, T. 2007. A computationally efficient model of convective heat transfer and solidification characteristics during keyhole mode laser welding. *Journal of Applied Physics* 101: article #054909.

22. Rai, R., Kelly, S. M., Martukanitz, R. P., and DebRoy, T. 2008. A convective heat-transfer model for partial and full penetration keyhole mode laser welding of a structural steel. *Metallurgical and Materials Transactions A* 39A (1): 98 to 112.

23. Rai, R., Elmer, J. W., Palmer, T. A., and DebRoy, T. 2007. Heat transfer and fluid flow during keyhole mode laser welding of tantalum, Ti–6Al–4V, 304L stainless steel and vanadium. *Journal of Physics D: Applied Physics* 40: 5753 to 5766.

24. Elmer, J. W., Giedt, W. H., and Eagar, T. W. 1990. The transition from shallow to deep penetration during electron-beam welding. *Welding Journal* 69(5): 167-s to 176-s.

25. Wei, P. S., and Giedt, W. H. 1985. Surface tension gradient-driven flow around an electron beam welding cavity. *Welding Journal* 64: 251-s to 259-s.

26. Wei, P. S., and Chow, Y. T. 1992. Beam focusing characteristics and alloying element effect on high-intensity electron beam welding. *Metallurgical Transactions B* 23B: 81 to 90.

27. Wei, P. S., Ho, C. Y., Shian, M. D., and Hu, C. L. 1997. Three-dimensional analytical temperature field and its application to solidification characteristics in high- or low-power-density beam welding. *International Journal of Heat and Mass Transfer* 40: 2283–2292.

28. Elmer, J. W., and Teruya, A. T. 1998. Fast method for measuring power-density distribution of non-circular and irregular electron *beams. Science and Technology of Welding and Joining* 3(2): 51-58.

29. Brandes, E. A., and Brook, G. B. 1992. *Smithells Metals Reference Book,* 7th ed., Butterworth Heinemann, Mass.

30. Schiller, S., Heisig, U., and Panzer, S. 1982. *Electron Beam Technology*, John Wiley and Sons, Berlin, Germany.

31. Kaye, G. W. C., and Laby, T. B. 1995. *Tables of Physical and Chemical Constants*, Longman, London, UK.

32. Lancaster, J. F. 1986. *The Physics of Welding*, Pergamon Press, Oxford, UK.

33. Bird, R. B., Stewart, W. E., and Lightfoot, E. N. 1960. *Transport Phenomena*, Wiley, New York, N.Y.

34. Patankar, S. V. 1980. *Numerical Heat Transfer and Fluid Flow*, Hemisphere Publishing Corporation, New York, N.Y..

35. Voller, V. R., and Prakash, C. 1987. A fixed grid numerical modelling methodology for convection-diffusion mushy region phase-change problems. *International Journal of Heat and Mass Transfer* 30: 1709–1720.

36. Brent, A. D., Voller, V. R., and Reid, K. J. 1988. Enthalpy-porosity technique for modeling convection-diffusion phase change: Application to the melting of a pure metal. *Numerical Heat Transfer* 13: 297–318.

37. Zhang, W., Kim, C. H., and DebRoy, T. 2004. Heat and fluid flow in complex joints during gas-metal arc welding, Part I: Numerical model of fillet welding. *Journal of Applied Physics* 95(9): 5210–5219.

38. Zhang, W., Kim, C. H., and DebRoy, T. 2004. Heat and fluid flow in complex joints during gas-metal arc welding, Part II: Application to *Fillet Welding of Mild Steel*. *Journal of Applied Physics* 95(9): 5220–5229

39. Kumar, A., and DebRoy, T. 2003. Calculation of Three-Dimensional Electromagnetic Force Field during Arc Welding. *Journal of Applied Physics* 94: 1267–1277.

40. Kou, S., and Sun, D. K. 1985. Fluid flow and weld penetration in stationary arc welds. *Metalurgical Transactions A* 16A: 203–213.

41. Kim, C. H., Zhang, W., and DebRoy, T. 2003. Modeling of temperature field and solidified surface profile during gas metal arc fillet welding. *Journal of Physics D: Applied Physics* 94: 2667–2679.

42. De, A., and DebRoy, T. 2004. Probing unknown welding parameters from convective heat transfer calculation and multivariable optimization. *Journal of Applied Physics* 37(1): 140–150.

43. De, A., and DebRoy, T. 2004. A smart model to estimate effective thermal conductivity and viscosity in weld pool. *Journal of Applied Physics* 95(9): 5230–5240.

44. DebRoy, T., and Majumdar, A. K. 1981. Predicting fluid flow in gas stirred systems. *Journal of Metals* 33(11): 42–47.

45. Launder, B. E., and Spalding, D. B. 1972. *Lectures in Mathematical Models of Turbulence,* Academic Press, London, UK.

46. Hong, K. 1996. Ph.D. dissertation, University of Waterloo.

47. Yang, Z., and DebRoy, T. 1999. Modeling of macro- and microstructures of gas-metal-arc welded HSLA-100 steel. *Metallurgical Transactions B* 30B: 483–493.

48. He, X., Elmer, J. W., and DebRoy, T. 2005. Heat T*ransfer and Fluid Flow in Laser Microwelding*. *Journal of Applied Physics* 97: article# 84909.